OPTICA

Entanglement swapping with spatially multiplexed modes in an atomic-ensemble quantum memory in a single excitation regime

Minjie Wang,[1,2] Haole Jiao,[1,2] Jiajin Lu,[1,2] Wenxin Fan,[1,2] Shujing Li,[1,2,3] and Hai Wang[1,2,*]

[1]State Key Laboratory of Quantum Optics Technologies and Devices, Institute of Opto-Electronics, Shanxi University, Taiyuan 030006, China
[2]Collaborative Innovation Center of Extreme Optics, Shanxi University, Taiyuan 030006, China
[3]lishujing@sxu.edu.cn
*wanghai@sxu.edu.cn

Received 13 August 2024; revised 14 January 2025; accepted 5 February 2025; published 19 February 2025

Entanglement swapping (ES) between memory repeater links is critical for establishing quantum networks via quantum repeaters. So far, ES with atomic-ensemble-based memories has not been achieved. Here, we experimentally demonstrate ES between different spatial modes for a cold-atom-ensemble quantum memory via the Duan-Lukin-Cirac-Zoller scheme. With a cloud of cold atoms inserted in a cavity, we produce non-classically correlated spin-wave-photon pairs in 12 spatial modes. We then prepare two entangled pairs of spin-wave modes through memory multiplexing. Via single-photon Bell-state measurement on retrieved fields from two spin-wave modes, we project the two remaining modes never entangled previously into an entangled state with a measured concurrence of $\mathcal{C} = 0.0124 \pm 0.0030$. The successful probability of ES in our scheme is increased by three times, compared with that in the scheme without memory multiplexing. Our presented work shows that the generation of entanglement ($\mathcal{C} > 0$) between the remaining spin-wave modes requires the average cross-correlation function of the spin-wave-photon pairs to be ≥ 30. This presented work represents a significant step toward practical quantum repeaters. © 2025 Optica Publishing Group under the terms of the Optica Open Access Publishing Agreement

https://doi.org/10.1364/OPTICA.539388

1. INTRODUCTION

Quantum networks [1,2] enable revolutionary applications including quantum simulation [3], computation [4], global quantum communication [5,6], highly accurate frequency comparisons [7], and long-baseline telescopes [8]. To establish global quantum networks, quantum repeaters (QRs) are essential [9–11]. In QRs, long distances are divided into a number of elementary links. Entanglement is independently generated in each link and then successively extended via entanglement swapping (ES) between two adjacent links.

Over the past two decades, researchers have demonstrated entanglement between two quantum memories, forming single elementary links, using various systems such as atomic ensembles [12–20], individual atoms [21–23], ions [24], and solid-state spins [25]. The first ES experiment was realized with entangled photons [26] via a Bell-state measurement (BSM). Since then, ES has been widely demonstrated with photons [27], continuous-variable light beams [28], and hybrid continuous-variable-discrete-variable optical system [29]. Recently, two-hierarchy entanglement swapping for QR has been demonstrated with four entangled pairs of photons [30]. Moreover, deterministic ES with single ions [31] or superconducting qubits [32] has been demonstrated via a quantum-logic-gate-based BSM.

Toward entanglement extensions in QRs, ES has been demonstrated with NV-center-based memories that interface photons via BSM on stationary qubits [33]. Recently, Pu *et al.* experimentally demonstrated ES between two hybrid entanglement states between a Stokes photon and an atomic-ensemble-based memory [34], where, the Stokes photons are projected into an entangled state by performing a BSM on two retrieved photons in a post-selected way. The experiment [34] indicated that the scaling rate of entanglement connection between two repeater links can be enhanced using long-lived memories [11,35–37]. However, even if one holds the memory-enhanced scaling, the rates of QRs are still slow for practicality [11,35,38]. To improve the QR rates, QRs using multiplexed memories with atomic ensembles [11,38–42], single ions [43], atomic arrays [44], and NV centers [45] have been proposed. Experimentally, the multimode quantum memories based on atomic ensembles have been demonstrated [41,42,46–53]. Heralded entanglement between two multimode quantum memories [16] or multiplexed quantum teleportation [52] from photon to memory has been demonstrated with solid-state ensembles. In 2007, Laurat *et al.* proceeded ES of quantum memories stored in two independently cold atomic ensembles based on a single-mode scheme [54]. The authors prepared two pairs of entangled quantum memories in an asynchronous fashion and then performed ES by performing a single-photon BSM on

retrieved fields from two memories. Unfortunately, they did not detect entanglement (concurrence $\mathcal{C} > 0$) between the remaining two memories due to decoherence of the memories. So far, ES with ensemble-based quantum memories remains elusive in experiments.

In the presented study, we demonstrate ES between spin waves stored in different spatial modes in a cloud of cold atoms, where the ES rate is enhanced through memory multiplexing. At first, we produce non-classically correlated pairs of a Stokes photon and a spin wave in 12 spatial modes via the Duan-Lukin-Cirac-Zoller (DLCZ) process. The multiple spin-wave modes are set to be as four ends A, B1, B2, and C, which are paired via Stokes interference and form two multiplexed links A-B1 and B2-C. Then, we simultaneously prepare two entangled states $\Psi_{A,B1}$ and $\Psi_{B2,C}$ in A-B1 and B2-C links via single-photon BSMs, respectively. After storage time t_1, the spin-wave modes in B1 and B2 ends are retrieved for ES via single-photon BSM. A successful BSM heralds the establishment of entangled state $\Psi_{A,C}$ between the remaining spin-wave modes in the A and C ends. At storage time t_2 ($>t_1$), we retrieve the entangled spin-wave modes in the A and C ends for entanglement verification. We measure the dependences of visibility V and suppression parameter h of the entangled state $\Psi_{A,C}$ on t_2. Due to spin-wave decoherence, $V(h)$ decreases (increases) with t_2. We also presented the dependence of concurrence ($\mathcal{C}$) of $\Psi_{A,C}$ on t_2, which shows that entanglement ($\mathcal{C}_{A,C} > 0$) can be achieved for a storage time during the ES process.

2. SCHEMATIC VIEW OF ES SCHEME WITH MULTIPLEXED SPIN-WAVE MODES

Figure 1 provides a schematic view of our experiment for ES between spin-wave modes in two links in a cold atomic ensemble, where, A, B1, B2, and C are the ends of the links. We use the DLCZ scheme to generate entangled states in the two links and subsequently perform ES. A write laser pulse is applied into the ensemble, inducing spontaneous Raman emissions of Stokes photons in space [42]. By collecting the Stokes photons in different directions (modes), we produce non-classically correlated pairs of a Stokes photon and a spin wave in 12 spatial modes. The 12 spin-wave modes are grouped into the A, B1, B2, and C ends, and the 12 Stokes modes are set into S_A, S_{B1}, S_{B2}, and S_C fields, which are used for connecting the ends via interference. Each end and each Stokes field include $m = 3$ multiplexed modes, for example, the end X (=A, B1, B2, or C) includes modes $X^{(i=1,2,3)}$, and the Stokes field S_X includes three modes $S_X^{(i=1,2,3)}$. The multiplexed modes promise us to improve ES rate by a factor of three. For simplicity, the multiplexed modes are drawn overlapping in Fig. 1. Each mode in the A, B1, B2, and C ends is defined by its wavevector, which is determined by the Stokes mode correlated with it [49,55]. The spin-wave modes in A, B1, B2, and C ends have distinguishable directions and are independently preserved. In Supplement 1, we explained how each spin-wave mode is associated with a sub-ensemble. In the entanglement generation step [Fig. 1(a)], the Stokes photons in the i-th mode of S_A (S_{B1}) and S_{B2} (S_C) fields are combined on a 50/50 beam splitter $BS_{EG1}^{(i)}$ ($BS_{EG2}^{(i)}$), the two outputs of which are directed to single-photon detectors $D_{EG1}^{(i)}$ and $D_{EG1}^{\prime(i)}$ ($D_{EG2}^{(i)}$ and $D_{EG2}^{\prime(i)}$), respectively, for single-photon BSM, where $i = 1, 2$ or 3. Note that in Fig. 1(a), the superscripts to $BS_{EG1}^{(i=1,2,3)}$ ($BS_{EG2}^{(i=1,2,3)}$) and $D_{EG1}^{(i)}$, $D_{EG1}^{\prime(i)}$, $D_{EG2}^{(i)}$, and $D_{EG2}^{\prime(i)}$ are omitted for simplicity. A detection event at $D_{EG1}^{(i)}$ ($D_{EG2}^{(i)}$) or $D_{EG1}^{\prime(i)}$ ($D_{EG2}^{\prime(i)}$) projects the i-th spin-wave modes in A and B1 (B2 and C) ends into an entangled state [54], meaning that the A and B1 (B2 and C) ends are entangled. The entangled states in the A-B1 and B2-C links are written as

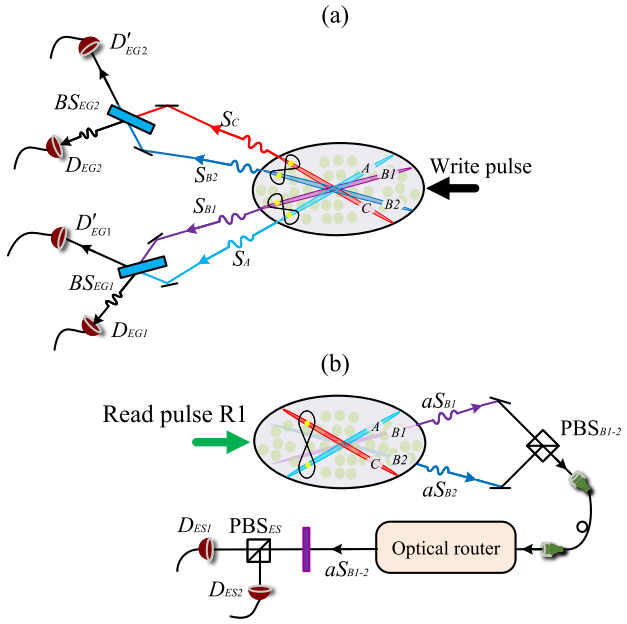

Fig. 1. Schematic view of the entanglement swapping with multiplexed spin-wave modes in an atomic ensemble. A, B1, B2, and C denote four ends, each of which includes three multiplexed spin-wave modes; S_A, S_{B1}, S_{B2}, and S_C denote the four Stokes fields, each of which includes three multiplexed modes. For simplicity, the multiplexed modes are drawn overlapping. (a) Entanglement generations in two multiplexed links A-B1 and B2-C via single-photon BSMs. (b) Entanglement swapping between the two links via interference between the retrieved fields from the B1 and B2 ends. BS_{EG1} and BS_{EG2}: 50/50 beam splitters; D_{EG1}, D'_{EG1}, D_{EG2}, D'_{EG2}, D_{ES1}, and D_{ES2}: single-photon detectors; PBS_{ES} and PBS_{B1-2}: polarization beam splitters.

$$\Psi_{A,B1} = \left(|1\rangle_A|0\rangle_{B1} \pm e^{-i\Delta\alpha_1}|0\rangle_A|1\rangle_{B1}\right)/\sqrt{2}, \quad (1a)$$

$$\Psi_{B2,C} = \left(|1\rangle_{B2}|0\rangle_C \pm e^{-i\Delta\alpha_2}|0\rangle_{B2}|1\rangle_C\right)/\sqrt{2}, \quad (1b)$$

respectively, where $\Delta\alpha_1 = \alpha_A - \alpha_{B1}$ ($\Delta\alpha_2 = \alpha_{B2} - \alpha_C$) denotes the phase difference between the i-th modes of the Stokes fields S_A and S_{B1} (S_{B2} and S_C) in the propagations from the spin-wave modes at A and B1 (B2 and C) ends to $BS_{EG1}^{(i)}$ ($BS_{EG2}^{(i)}$). In this presented ES scheme, the relative phases $\Delta\alpha_1^{(i)}$($\Delta\alpha_2^{(i)}$) for the A-B1 (B2-C) link established between the i-th modes are passively and well stabilized as a fixed constant $\Delta\alpha_1$ ($\Delta\alpha_2$), i.e., $\Delta\alpha_1^{(i=1,2,3)} = \Delta\alpha_1$ ($\Delta\alpha_2^{(i=1,2,3)} = \Delta\alpha_2$). In the presented ES, only the two entangled states that are established between the i-th modes in the A-B1 and B2-C links in a synchronous fashion can be used for the next ES step. The reason for this is explained below. Limited by the presented ES scheme, the probability of simultaneously generating the two entangled states is proportional to $3\chi^2$, where χ is the probability to generate the spin-wave-photon pair in an individual mode.

After storage time t_1, we convert the i-th spin-wave modes in B1 and B2 ends into two anti-Stokes modes aS_{B1}^i and aS_{B2}^i, respectively, using a read laser pulse R1. This ES step is illustrated in Fig. 1(b), where the multiplexed modes are simplified as aS_{B1}

and aS_{B2}. Determined by the phase match condition [49,55], the retrieved anti-Stokes modes $aS_{B1}^{(i)}$ and $aS_{B2}^{(i)}$ propagate in the opposite direction to the modes $S_{B1}^{(i)}$ and $S_{B2}^{(i)}$, respectively. We use polarizer $\mathrm{PBS}_{B1,2}^{(i)}$ [simplified as PBS_{B1-2} in Fig. 1(b)], to combine the retrieved modes into a spatial mode $aS_{B1-2}^{(i)}$, where $i = 1$, 2 or 3. Such spatial mode includes H-polarization $aS_{B1}^{(i)}$ and V-polarization $aS_{B2}^{(i)}$ components retrieved from the spin waves stored in $B1^{(i)}$ and $B2^{(i)}$ modes. The $aS_{B1-2}^{(i)}$ mode is sent to an optical router. For experimental trials, the mode $aS_{B1-2}^{(i=12\,\mathrm{or}\,3)}$ is routed into a common channel aS_{B1-2} by feed-forward controlled signals. The mode aS_{B1-2} goes through a $\lambda/2$-plate and a polarization beam splitter PBS_{ES}. The output fields $(a_{aS_{B1}^{(i)}} \pm e^{i\Delta\gamma_i} a_{aS_{B2}^{(i)}})/\sqrt{2}$ of PBS_{ES} are directed into detectors D_{ES1} and D_{ES2}, respectively, where $a_{aS_{B1}^{(i)}}$ ($a_{aS_{B2}^{(i)}}$) denotes the annihilation operator associated with the field $aS_{B1}^{(i)}$ ($aS_{B2}^{(i)}$), and $\Delta\gamma^{(i)}$ the relative phase between the anti-Stokes modes $aS_{B1}^{(i)}$ and $aS_{B2}^{(i)}$ from the spin-wave modes $B1^{(i)}$ and $B2^{(i)}$ to the PBS_{ES}, which is required to be stabilized in ES. In our scheme, we perform ES operation on a pair of fixed anti-Stokes modes $aS_{B1}^{(i)}$ and $aS_{B2}^{(i)}$ (i = 1, 2 or 3). Thus, the relative phase $\Delta\gamma^{(i)}$ for different mode pairs is passively stabilized as a fixed constant, i.e., $\Delta\gamma^{(i=1,2,3)} = \Delta\gamma$, thereby decreasing the experimental complexities. However, this scheme with its retrieved anti-Stokes modes being pairwise-fixed results in that two entangled states are established between the i-th modes in links A-B1 and B2-C, as mentioned above. Returning to the ES scheme in Fig. 1(b), a detection event at D_{ES1} or D_{ES2} indicates a successful BSM, which projects the remaining spin-wave modes in the A and C ends into the state [54]

$$\rho_{A,C} = |0\rangle\langle 0|/2 + |\Psi_{A,C}\rangle\langle\Psi_{A,C}|/2, \tag{2}$$

where

$$\Psi_{A,C} = \left(|1\rangle_A|0\rangle_C \pm e^{-i\xi}|0\rangle_A|1\rangle_C\right)/\sqrt{2} \tag{3}$$

is the entangled state between A and C, $|0\rangle$ is the vacuum part, and $\xi = \Delta\alpha_1 + \Delta\alpha_2 + \Delta\gamma$ is the sum of the relative phases.

3. EXPERIMENTAL SCHEME

The experimental setup [Fig. 2(a)] comprises a cloud of cold ^{87}Rb atoms coupled to a ring cavity with a finesse of ∼16 and free spectral range of 50 MHz. To enhance spin-wave retrieval efficiencies [55–57], this cavity is a spatially multiplexed cavity [58] that simultaneously resonates with the 12 TEM_{00} modes, which are labeled as $T_A^{(i)}$, $T_{B1}^{(i)}$, $T_{B2}^{(i)}$, and $T_C^{(i)}$ ($i = 1$ to 3). Note that Fig. 2(a) is a view from the top for which the modes $T_X^{(i=1\mathrm{to}3)}$ (X = A, B1, B2, C) overlap.

We carry out the ES experiment in a cyclic fashion. In the beginning of a trial, the atoms are released from a magneto-optical trap (MOT) and are prepared in the Zeeman state $|a, m_F = 0\rangle$. By applying a 795 nm write pulse red-detuned by 110 MHz to the $|a\rangle \to |e_1\rangle$ transition [see Fig. 2(b)], we create spontaneous Raman emissions of Stokes photons on the $|e_1\rangle \leftrightarrow |b\rangle$ transition. Specifically, the write pulse is σ^+-polarized and is directed into the atoms through a beam splitter BS_W along z-axis. It induces the σ^+-polarized Stokes-photon emissions on the transition $|e_1, m_F = +1\rangle \leftrightarrow |b, m_F = 0\rangle$ or σ^--polarized Stokes photon on the transition $|e_1, m_F = +1\rangle \leftrightarrow |b, m_F = +2\rangle$, and simultaneously creates spin waves associated with Zeeman coherence $|a, m_F = 0\rangle \to |b, m_F = 0\rangle$ or $|a, m_F = 0\rangle \to |b, m_F = +2\rangle$. When a σ^-- (σ^+) polarized Stokes photon is emitted into the $T_A^{(i)}$ or $T_C^{(i)}$ ($T_{B1}^{(i)}$ or $T_{B2}^{(i)}$) cavity mode and propagates along counterclockwise (z-axis), it will be collected into entanglement-generation detection system as shown in Fig. 2(d) and then is taken as Stokes photon $S_A^{(i)}$ or $S_C^{(i)}$ ($S_{B1}^{(i)}$ or $S_{B2}^{(i)}$). Along with the creation of a photon in the $S_A^{(i)}$, $S_{B1}^{(i)}$, $S_{B2}^{(i)}$, or $S_C^{(i)}$ mode, one collective excitation is created and stored in the mode $A^{(i)}$, $B1^{(i)}$, $B2^{(i)}$, or $C^{(i)}$ with their wave-vectors defined by $k_{A,B1,B2,C}^{(i)} = k_w - k_{T_{A,B1,B2,C}}^{(i)}$, where k_w denotes the wave-vector of the write pulse and $k_{T_{A,B1,B2,C}}^{(i)}$ that of the Stokes photon propagating in one of the 12 cavity modes. The spin waves $A^{(i)}$ and $C^{(i)}$ ($B1^{(i)}$ and $B2^{(i)}$) are associated with the coherence $|a, m_F = 0\rangle \to |b, m_F = 0\rangle$ ($|a, m_F = 0\rangle \to |b, m_F = +2\rangle$). The probability of generating the spin-wave-photon pair in each of 12 modes is set to $\chi \sim 1\%$, which is far less than one in order to avoid multi-excitations [11]. The intrinsic retrieval efficiencies of the 12 spin-wave modes are all beyond ∼65% (see Supplement 1 for the measured raw data). On the left of the atoms, we insert a quarter-wave plate to transform σ^- (σ^+) -polarized Stokes photons propagating in the modes $T_A^{(i)}$ and $T_C^{(i)}$ ($T_{B1}^{(i)}$ and $T_{B2}^{(i)}$) into V- (H-) polarized ones, where $i = 1$ to 3. As shown in Fig. 2(a), the Stokes photon in the $T_X^{(i)}$ modes may escape from the cavity through the optical coupler (OC) and is directed into the $S_X^{(i)}$ mode. The V-polarized $S_A^{(i)}$ ($S_C^{(i)}$) and H-polarized $S_{B1}^{(i)}$ ($S_{B2}^{(i)}$) fields are combined at a beam displacer (BD1), then coupled into a single-mode fiber $\mathrm{SMF}_{A-B1}^{(i)}$ ($\mathrm{SMF}_{B2-C}^{(i)}$) and sent to the entanglement-generation (EG) detection system for single-photon BSM [Fig. 2(d)]. Upon the detection events simultaneously occurring at the detectors $D_{EG1}^{(i)}$ and $D_{EG3}^{(i)}$ ($i = 1$, 2 or 3), the entangled states $\Psi_{A,B1}$ and $\Psi_{B2,C}$ [see Eqs. (1a) and (1b)] for the A-B1 and B2-C multiplexed links are generated, respectively.

After a storage time t_1, we apply a σ^+-polarized read pulse $R1$ to convert both the spin waves B1 and B2 into anti-Stokes fields, which propagate in $T_{B1}^{(i)}$ and $T_{B2}^{(i)}$ cavity modes along clockwise [58], respectively. Escaping from the cavity mirror OC, the anti-Stokes fields in $T_{B1}^{(i)}$ and $T_{B2}^{(i)}$ modes are directed into $aS_{B1}^{(i)}$ and $aS_{B2}^{(i)}$ channels, which are H-polarized and V-polarized, respectively. We then use a beam displacer labeled as BD2 to combine $aS_{B1}^{(i)}$ and $aS_{B2}^{(i)}$ fields into a spatial mode $aS_{B1-2}^{(i)}$. The mode $aS_{B1-2}^{(i)}$ is coupled into single-mode fiber $\mathrm{SMF}_{B1-2}^{(i)}$. After passing through $\mathrm{SMF}_{B1-2}^{(i)}$, the $aS_{B1-2}^{(i=1\,\mathrm{to}\,3)}$ modes (each of which includes H- and V-polarization components) are sent to an optical switch network (OSN_1) [49] for their circuit multiplexing. Based on feed-forward controlled signals, the $aS_{B1-2}^{(i=1,2\mathrm{or}3)}$ mode, whose H- and V-components are retrieved from the spin waves stored in $B1^{(i)}$ and $B2^{(i)}$ modes, respectively, is routed into a common single-mode fiber (CSMF_1) by the OSN1, which is labeled as aS_{B1-2} mode. Passing through CSMF_1, the aS_{B1-2} mode, the H-polarized and V-polarized components of which are used for aS_{B1} and aS_{B2} fields, respectively, goes through a $\lambda/2$-plate and is directed to a polarization beam splitter (PBS_{ES}). Its outputs are sent to the single-photon detectors D_{ES1} and D_{ES2} [Fig. 2(e)], respectively. Upon a detection event at D_{ES1} [54,55], the remaining

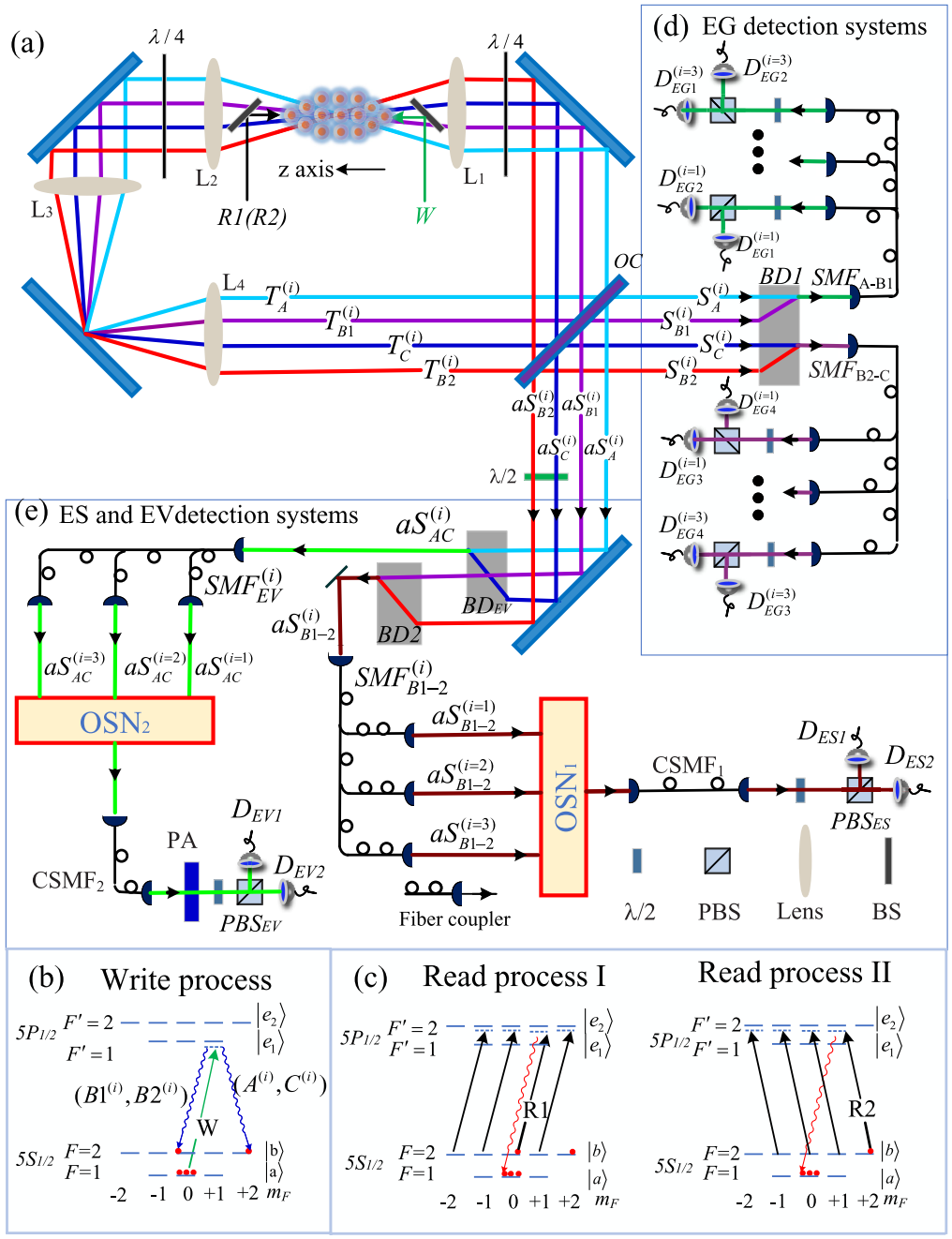

Fig. 2. Experimental setup. (a) The spatially multiplexed source of generating the spin-wave-photon pairs. The source is formed by a cloud of Rb atoms inserted in a ring cavity. The cavity supports 12 TEM_{00} modes, labeled $T_A^{(i)}$, $T_{B1}^{(i)}$, $T_{B2}^{(i)}$, and $T_C^{(i)}$ cavity modes, with $i = 1, 2, 3$. (a) Top view of the source, meaning that we only plot four lines, labeled by $T_A^{(i)}$, $T_{B1}^{(i)}$, $T_{B2}^{(i)}$, and $T_C^{(i)}$. A bias magnetic field (100 mG) is applied along z-direction to define the quantum axis. (b), (c) Relevant levels of the ^{87}Rb atoms for the write and read processes. (d) The detection systems for entanglement generation (EG) of the two entangled spin-wave pairs. (e) The detection systems for performing entanglement swapping (ES) and entanglement verification (EV). In the main text, we describe in detail the Stokes optical circuits in (d) and anti-Stokes circuits in (e). Before each polarization beam splitter (PBS), we place a half-wave plate ($\lambda/2$) set at 22.5°. Thus, the H- and V-polarized Stokes (anti-Stokes) fields are 50/50 mixed at the two PBS outputs. The PBSs in this figure are used as the corresponding BSs in Fig. 1. In (e) and (d), the length of each fiber is about 10 m. OSN: optical switch network, BD: beam displacer, SMF: single-mode fiber, CSMF: common single-mode fiber, BS: beam splitter, PA: phase adjustment, OC: optical coupler.

spin-waves modes in A and C ends are projected into the entangled state $\Psi_{A,C}$ described by Eq. (3).

In our presented experiment, the sum of the relative phases $\xi = \Delta\alpha_1 + \Delta\alpha_2 + \Delta\gamma$ is passively stabilized. The entanglement degree of the state $\Psi_{A,C}$ can be characterized by the concurrence [12,18]

$$\mathcal{C} = \max\{0, \left((P_{10} + P_{01})\, V_{AC} - 2\sqrt{P_{00}\, P_{11}}\right)/P$$
$$\approx \max\left\{0,\, P_c\left(V_{AC} - \sqrt{h}\right)\right\}, \quad (4)$$

where V_{AC} denotes the visibility of interference between the retrieved (anti-Stokes) fields $a\,S_A$ and $a\,S_C$ retrieved from the spin waves stored in the A and C modes, P_{ij} is the probability to find

$i \in (0, 1)$ photons in the retrieved field aS_A and $j \in (0, 1)$ photons in the retrieved field aS_C, $P = P_{10} + P_{01} + P_{11} + P_{00} \approx 1$, $h = P_{11}/(P_{10}P_{01}) < 1$ denotes the suppression parameter of two-photon events relative to the square of the probability of single-photon events [12], $P_c = P_{10} + P_{01} \approx 2P_{10} \approx 2P_{01}$, and the concurrence $\mathcal{C}$ takes values from zero for a separable state to one for a maximally entangled state.

We next make the detailed theoretical analyses on the dependence of the visibility V_{AC} as well as suppression parameter h_{AC} on the cross-correlation functions of the spin-wave-photon pairs in Supplement 1 and present the main results:

$$V_{AC} \approx 1 - 4/g_{S,aS}(t_1) - 4/g'_{S,aS}(t_2), \tag{5a}$$

$$h_{AC} \approx 8 \times \left(1/g_{S,aS}(t_1) + 1/g'_{S,aS}(t_2)\right), \tag{5b}$$

where $g_{S,aS}(t_1)$ ($g_{S,aS'}(t_2)$) denotes the cross-correlation function for either one of the spin-wave-photon pairs from spin-wave modes B1 (A) and B2 (C) at time $t_1(t_2)$, with $g^{(B1)}_{S,aS}(t_1) = g^{(B2)}_{S,aS}(t_1) = g_{S,aS}(t_1)$ ($g^{(A)}_{S,aS}(t_2) = g^{(C)}_{S,aS}(t_2) = g'_{S,aS}(t_2)$) assumed. With Eqs. (4) and (5), we calculate the threshold of the cross-correlations $g_{S,aS}$ to generate entanglement (the concurrence $\mathcal{C} \geq 0$) between the two remaining spin-wave modes, which is $g_{S,aS} \approx 29.3$.

To measure the concurrence $\mathcal{C}_{AC}$ of the entangled state $\Psi_{A,C}$, we apply a σ^--polarized read pulse $R2$ at the storage time t_2 ($t_2 = t_1 + \Delta t$) to convert the modes in A and C ends into anti-Stokes fields, which are H- and V-polarized and propagate in $T^{(i)}_A$ and $T^{(i)}_C$ modes along clockwise, respectively. The anti-Stokes fields in $T^{(i)}_A$ and $T^{(i)}_C$ modes escape from the cavity OC, which then are directed into $aS^{(i)}_A$ and $aS^{(i)}_C$ modes, respectively. The H- and V-polarized fields $aS^{(i)}_A$ and $aS^{(i)}_C$ are combined into the spatial mode $aS^{(i)}_{AC}$ by a beam displacer labeled as BD_{EV}. The $aS^{(i)}_{AC}$ mode, which includes H- and V-polarized fields ${aS_A}^{(i)}$ and ${aS_C}^{(i)}$, is coupled into the single-mode fiber $SMF^{(i)}_{EV}$ and then sent to another optical switch network OSN_2. Based on feed-forward controlled signals [48], the $aS^{(i)}_{AC}$ mode ($i = 1$, 2 or 3), whose H- and V-polarized fields ${aS_A}^{(i)}$ and ${aS_C}^{(i)}$ are retrieved from the i-th modes of the A and C ends, respectively, is routed into a common single-mode fiber ($CSMF_2$) by the OSN_2. After the CSMF2, this $aS^{(i)}_{AC}$ mode serves as aS_{AC}. The aS_{AC} mode goes through a phase adjustment (PA) [20] that varies the relative phase θ between the H-polarized aS_A and V-polarized aS_C fields. The mode aS_{AC} is then sent to an entanglement-verification detection system, which includes a $\lambda/2$ plate, a polarization beam splitter (PBS_{EV}) and two single-photon detectors D_{EV1} and D_{EV2} [Fig. 2(e)]. The outputs of PBS_{EV} are $(aS_A \pm e^{i\theta} aS_C)/\sqrt{2}$ fields, which are directed into D_{EV1} and D_{EV2} detectors, respectively.

The visibility V_{AC} is measured by recording the counts N_{EV1} at D_{EV1} (N_{EV2} at D_{EV2}) conditioned on a successful ES (an event at the detector D_{ES1}) when θ is scanned. Figure 3 shows the measured conditional counts N_{EV1}, N_{EV2} as functions of θ for the storage time $t_1 = 0$, $t_2 = t_1 + \Delta t = 2$ μs. From the measured data, we find the visibility to be $V_{AC} = 0.74 \pm 0.03$.

Conditioned on successful ES events, we measure the probabilities P_{ij} by detecting photon counts in the aS_A and aS_C fields for the storage time $t_1 = 0$, $t_2 = 2$ μs. The measured results are shown in Table 1, from which we give a suppression parameter $h_{AC} = P_{11}/(P_{10}P_{01}) = 0.36 \pm 0.06$.

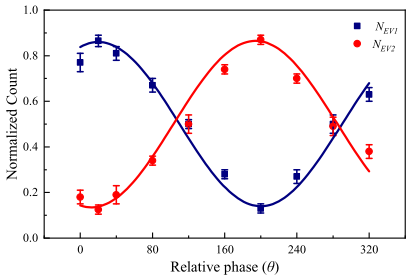

Fig. 3. Measured conditional counts N_{EV1} and N_{EV2} by the detectors D_{EV1} and D_{EV2}, respectively, as functions of θ for $t_1 = 0$, $t_2 = 2$ μs, which present interference fringes. The error bars represent one standard deviation.

Table 1. Measured Probabilities P_{ij} at $t_1 = 0$, $t_2 = 2$ μs (error bars represent one standard deviation)

P_{00}	$(92.51 \pm 0.30) \times 10^{-2}$
P_{10}	$(2.97 \pm 0.10) \times 10^{-2}$
P_{01}	$(4.55 \pm 0.10) \times 10^{-2}$
P_{11}	$(4.90 \pm 0.80) \times 10^{-4}$

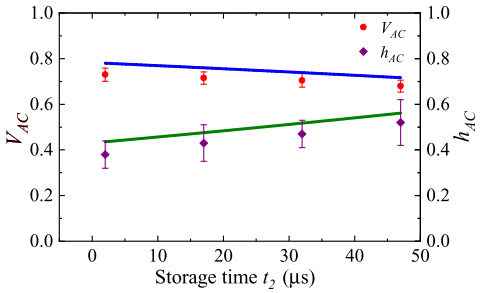

Fig. 4. Measured V_{AC} (red circles) and h_{AC} (purple diamonds) as a function of the storage time t_2 ($t_2 = t_1 + 2$ μs), which is changed by varying the time t_1, where the delay Δt is fixed at 2 μs; t_1 is the time at which we perform ES. The error bars represent one standard deviation.

Furthermore, we measure V_{AC} and h_{AC} at different storage times t_2 (see Supplement 1 for detailed raw data). We obtain V_{AC} (red circles) and h_{AC} (purple diamonds) values from the raw data and plot them in Fig. 4, which show that V_{AC} (h_{AC}) decreases (increases) with the storage time t_2. The solid curves in Fig. 4 are the fits to the measured V_{AC} and h_{AC} data according to Eqs. (5a) and (5b), respectively. For these fits, the data of $g_{S,aS}(t_1)$, $g'_{S,aS}(t_2)$ are taken from fits to the measured $g_{S,aS}(t_1)$, $g'_{S,aS}(t_2)$ data, which are presented in Fig. S3 in Supplement 1. One can see that the fittings curves in Fig. 3 are in agreement with the measured V_{AC} and h_{AC} data. We attribute the decrease (increase) in V_{AC} (h_{AC}) to the spin-wave decoherence.

Based on the measured V_{AC} and h_{AC} data as well as $P_c = P_{10} + P_{01}$ for aS_{AC} fields, we present the concurrence $\mathcal{C}_{AC}$ (blue squares) as a function of the storage time t_2 in Fig. 5, which shows that $\mathcal{C}_{AC}$ decreases with t_2. The solid red curve is the fit to the measured $\mathcal{C}_{AC}$ data according to the relationship described by Eq. (S40) in Supplement 1. The measured maximal $\mathcal{C}_{AC}$ (at $t_2 \approx 2$ μs) in Fig. 5 is 0.0124 (<1), which is mainly limited by background noise, low detection, and optical coupling efficiencies. The concurrence (0.0023 ± 0.0020) is slightly above zero at $t_2 = 32$ μs, which corresponds to cutoff time t_{cut} [59], i.e., the system's storage time. At this cutoff time ($t_{\text{cut}} = t_2 \approx 32$ μs), the

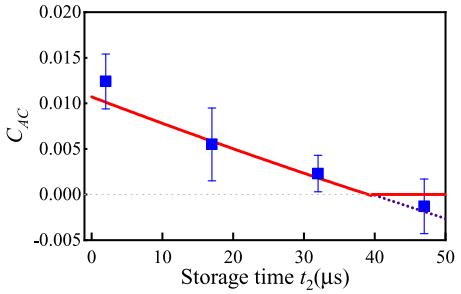

Fig. 5. Measured concurrence $\mathcal{C}_{AC}$ (blue squares) as a function of the storage time t_2. The error bars represent one standard deviation.

average $g_{S,aS}(t_1)$ and $g'_{S,aS}(t_2)$ are ∼30 [Fig. S3 in Supplement 1), which is basically in agreement with the threshold $g_{S,aS} \approx 29.3$. The cutoff time is mainly limited by decoherence of the four spin waves (see Figs. S1 and S2 in Supplement 1). By loading the cold atoms into an optical lattice [56], one may suppress the decoherence and obtain a long cutoff time.

We subsequently measure four-photon coincidence counts between the detectors D_{EG1}, D_{EG3}, D_{ES1}, D_{EV1} as a function of the number of the multiplexed modes m (see Fig. S4 in Supplement 1). The measured data, which correspond to the rates of ES, present a linear increase with m and show a three-fold increase for maximum $m = 3$.

4. CONCLUSION

We have demonstrated ES between two pairs of entangled spin-wave modes in a cloud of cold atoms. The spin-wave modes are individually stored (Supplement 1), and ES is performed in a heralded way. The uses of the memory multiplexing and the cavity-enhanced retrievals enable the ES rate to be effectively enhanced. Then, we select a low excitation probability $\chi \approx 1\%$ and start ES with a large average value $g_{S,aS} \sim 40$ (see Fig. S3 for details). The large value of $g_{S,aS}$ is the key feature to realize ES between the spin waves. We note that the entanglement connection between entangled spin-wave-photon pairs has been demonstrated with multi-cell memories [53], where signal photons instead of spin waves are projected into an entangled state. In our presented experiment, the measured concurrence of the entanglement state between the remaining spin-wave modes is $\mathcal{C}_{AC} = 0.0124 \pm 0.0030$ at 2 μs delay, which violates the inequality $\mathcal{C} \geq 0$ by 4.1 standard deviations. We present the first demonstration of the decay of the resultant entanglement state $\psi_{A,C}$ with storage time t during the ES process, which shows that the resultant entanglement ($\mathcal{C}_{A,C} > 0$) is achieved for a storage time (cutoff) of ∼32 μs. The quantitative relationship between the cross-correlation functions ($g_{S,aS}(t)$) of the spin-wave-photon pairs and the concurrence $\mathcal{C}_{A,C}$ presented by us is well in agreement with the measured data in Fig. 5 showing that the achievement of $\mathcal{C}_{A,C} > 0$ requires the average $\bar{g}_{S,aS}$ to exceed a threshold of ∼30. Such a threshold is four times the threshold $\bar{g}_{S,aS} \approx 7$ required for generating the single links [18,60], which shows that successful ES requires spin-wave-photon pairs to have higher quantum correlations. Our study shows that the cutoff time is mainly determined by the decay of $\bar{g}_{S,aS}$ with the storage time. Through memory multiplexing, our experiment demonstrates a three-fold increase in the ES rate, which shows the potential of multimode storage in improving the quantum repeater rate. The mode number in our presented setup is 12, which is mainly limited to sizes (∼50 mm) of the optical elements in the cavity. By increasing the element sizes to 150 mm, the number of modes will reach ∼120. ES between two or more repeater links over metropolitan fibers is now envisioned [5,61]. Aiming at this goal, quantum memories must have high-performances, including long lifetimes [53], low background noise, high detection and coupling efficiencies, massively multiplexed storages [46], quantum-frequency conversion [15,17,22], etc. Additionally, entanglement purification is required for the ES. In summary, our experimental results can be applied in the implementation of ES in practical QRs based on DLCZ-type schemes.

Funding. Key Project of the Ministry of Science and Technology of the People's Republic of China (2016YFA0301402); National Natural Science Foundation of China (12174235); Fund for Shanxi Key Subjects Construction (1331); Fundamental Research Program of Shanxi Province (202203021221011).

Acknowledgment. We thank Q. Zhou for helpful discussions.

Disclosures. The authors declare no conflicts of interest.

Data availability. Data may be obtained from the authors upon reasonable request.

Supplemental document. See Supplement 1 for supporting content.

REFERENCES

1. H. J. Kimble, "The quantum internet," Nature **453**, 1023–1030 (2008).
2. S. Wehner, D. Elkouss, and R. Hanson, "Quantum internet: a vision for the road ahead," Science **362**, 303 (2018).
3. K. S. Choi, A. Goban, S. B. Papp, *et al.*, "Entanglement of spin waves among four quantum memories," Nature **468**, 412–416 (2010).
4. L. Jiang, J. M. Taylor, A. S. Sørensen, *et al.*, "Distributed quantum computation based on small quantum registers," Phys. Rev. A **76**, 062323 (2007).
5. C. Simon, "Towards a global quantum network," Nat. Photonics **11**, 678–680 (2017).
6. S. H. Wei, B. Jing, X. Y. Zhang, *et al.*, "Towards real-world quantum networks: a review," Laser Photonics Rev. **16**, 2100219 (2022).
7. P. Kómár, E. M. Kessler, M. Bishof, *et al.*, "A quantum network of clocks," Nat. Phys. **10**, 582–587 (2014).
8. D. Gottesman, T. Jennewein, and S. Croke, "Longer-baseline telescopes using quantum repeaters," Phys. Rev. Lett. **109**, 070503 (2012).
9. H. J. Briegel, W. Dür, J. I. Cirac, *et al.*, "Quantum repeaters: the role of imperfect local operations in quantum communication," Phys. Rev. Lett. **81**, 5932 (1998).
10. L. M. Duan, M. D. Lukin, J. I. Cirac, *et al.*, "Long-distance quantum communication with atomic ensembles and linear optics," Nature **414**, 413–418 (2001).
11. N. Sangouard, C. Simon, H. de Riedmatten, *et al.*, "Quantum repeaters based on atomic ensembles and linear optics," Rev. Mod. Phys. **83**, 33–80 (2011).
12. C. W. Chou, H. de Riedmatten, D. Felinto, *et al.*, "Measurement-induced entanglement for excitation stored in remote atomic ensembles," Nature **438**, 828–832 (2005).
13. C.-W. Chou, J. Laurat, H. Deng, *et al.*, "Functional quantum nodes for entanglement distribution over scalable quantum networks," Science **316**, 1316–1319 (2007).
14. I. Usmani, C. Clausen, F. Bussiéres, *et al.*, "Heralded quantum entanglement between two crystals," Nat. Photonics **6**, 234–237 (2012).
15. Y. Yu, F. Ma, X. Y. Luo, *et al.*, "Entanglement of two quantum memories via fibres over dozens of kilometres," Nature **578**, 240–245 (2020).
16. D. Lago-Rivera, S. Grandi, J. V. Rakonjac, *et al.*, "Telecom-heralded entanglement between multimode solid-state quantum memories," Nature **594**, 37–40 (2021).
17. J.-L. Liu, X.-Y. Luo, Y. Yu, *et al.*, "A multinode quantum network over a metropolitan area," arXiv (2023).
18. J. Laurat, K. S. Choi, H. Deng, *et al.*, "Heralded entanglement between atomic ensembles: preparation, decoherence, and scaling," Phys. Rev. Lett. **99**, 180504 (2007).

19. M. Cao, F. Hoffet, S. Qiu, *et al.*, "Efficient reversible entanglement transfer between light and quantum memories," Optica **7**, 1440 (2020).
20. C. Sun, Y. Li, Y. Hou, *et al.*, "Decoherence of single-excitation entanglement over Duan-Lukin-Cirac-Zoller quantum networks caused by slow-magnetic-field fluctuations and protection approach," Adv. Quantum Technol. **6**, 2300148 (2023).
21. S. Ritter, C. Nolleke, C. Hahn, *et al.*, "An elementary quantum network of single atoms in optical cavities," Nature **484**, 195–200 (2012).
22. T. van Leent, M. Bock, F. Fertig, *et al.*, "Entangling single atoms over 33 km telecom fibre," Nature **607**, 69–73 (2022).
23. D. L. Moehring, P. Maunz, S. Olmschenk, *et al.*, "Entanglement of single-atom quantum bits at a distance," Nature **449**, 68–71 (2007).
24. V. Krutyanskiy, M. Galli, V. Krcmarsky, *et al.*, "Entanglement of trapped-ion qubits separated by 230 meters," Phys. Rev. Lett. **130**, 050803 (2023).
25. A. Delteil, Z. Sun, W. b. Gao, *et al.*, "Generation of heralded entanglement between distant hole spins," Nat. Phys. **12**, 218–223 (2015).
26. J.-W. Pan, D. Bouwmeester, H. Weinfurter, *et al.*, "Experimental entanglement swapping: entangling photons that never interacted," Phys. Rev. Lett. **80**, 3891 (1998).
27. M. Halder, A. Beveratos, N. Gisin, *et al.*, "Entangling independent photons by time measurement," Nat. Phys. **3**, 692–695 (2007).
28. X. Jia, X. Su, Q. Pan, *et al.*, "Experimental demonstration of unconditional entanglement swapping for continuous variables," Phys. Rev. Lett. **93**, 250503 (2004).
29. G. Guccione, T. Darras, H. L. Jeannic, *et al.*, "Connecting heterogeneous quantum networks by hybrid entanglement swapping," Sci. Adv. **6**, eaba4508 (2020).
30. P. Xu, H.-L. Yong, L.-K. Chen, *et al.*, "Two-hierarchy entanglement swapping for a linear optical quantum repeater," Phys. Rev. Lett. **119**, 170502 (2017).
31. M. Riebe, T. Monz, K. Kim, *et al.*, "Deterministic entanglement swapping with an ion-trap quantum computer," Nat. Phys. **4**, 839–842 (2008).
32. W. Ning, X.-J. Huang, P.-R. Han, *et al.*, "Deterministic entanglement swapping in a superconducting circuit," Phys. Rev. Lett. **123**, 060502 (2019).
33. M. Pompili, S. L. N. Hermans, S. Baier, *et al.*, "Realization of a multinode quantum network of remote solid-state qubits," Science **372**, 259–264 (2021).
34. Y. F. Pu, S. Zhang, Y. K. Wu, *et al.*, "Experimental demonstration of memory-enhanced scaling for entanglement connection of quantum repeater segments," Nat. Photonics **15**, 374–378 (2021).
35. N. Sangouard, C. Simon, B. Zhao, *et al.*, "Robust and efficient quantum repeaters with atomic ensembles and linear optics," Phys. Rev. A **77**, 062301 (2008).
36. M. Razavi, M. Piani, and N. Lütkenhaus, "Quantum repeaters with imperfect memories: Cost and scalability," Phys. Rev. A **80**, 032301 (2009).
37. N. Sangouard, C. Simon, J. Minář, *et al.*, "Long-distance entanglement distribution with single-photon sources," Phys. Rev. A **76**, 050301 (2007).
38. C. Simon, H. de Riedmatten, and M. Afzelius, "Temporally multiplexed quantum repeaters with atomic gases," Phys. Rev. A **82**, 010304 (2010).
39. C. Simon, H. de Riedmatten, M. Afzelius, *et al.*, "Quantum repeaters with photon pair sources and multimode memories," Phys. Rev. Lett. **98**, 190503 (2007).
40. O. A. Collins, S. D. Jenkins, A. Kuzmich, *et al.*, "Multiplexed memory-insensitive quantum repeaters," Phys. Rev. Lett. **98**, 060502 (2007).
41. N. Sinclair, E. Saglamyurek, H. Mallahzadeh, *et al.*, "Spectral multiplexing for scalable quantum photonics using an atomic frequency comb quantum memory and feed-forward control," Phys. Rev. Lett. **113**, 053603 (2014).
42. L. Tian, Z. Xu, L. Chen, *et al.*, "Spatial multiplexing of atom-photon entanglement sources using feedforward control and switching networks," Phys. Rev. Lett. **119**, 130505 (2017).
43. V. Krutyanskiy, M. Canteri, M. Meraner, *et al.*, "Multimode ion-photon entanglement over 101 kilometers," PRX Quantum **5**, 020308 (2024).
44. Y. Y. Li and J. D. Thompson, "High-rate and high-fidelity modular interconnects between neutral atom quantum processors," arXiv (2024).
45. S. B. v. Dam, P. C. Humphreys, F. Rozpedek, *et al.*, "Multiplexed entanglement generation over quantum networks using multi-qubit nodes," Quantum Sci. Technol. **2**, 034002 (2017).
46. E. Saglamyurek, M. Grimau Puigibert, Q. Zhou, *et al.*, "A multiplexed light-matter interface for fibre-based quantum networks," Nat. Commun. **7**, 11202 (2016).
47. A. Seri, D. Lago-Rivera, A. Lenhard, *et al.*, "Quantum storage of frequency-multiplexed heralded single photons," Phys. Rev. Lett. **123**, 080502 (2019).
48. Y. F. Pu, N. Jiang, W. Chang, *et al.*, "Experimental realization of a multiplexed quantum memory with 225 individually accessible memory cells," Nat. Commun. **8**, 15359 (2017).
49. S.-Z. Wang, M.-J. Wang, Y.-F. Wen, *et al.*, "Long-lived and multiplexed atom-photon entanglement interface with feed-forward-controlled readouts," Commun. Phys. **4**, 168 (2021).
50. K. C. Cox, D. H. Meyer, Z. A. Castillo, *et al.*, "Spin-wave multiplexed atom-cavity electrodynamics," Phys. Rev. Lett. **123**, 263601 (2019).
51. M. Businger, L. Nicolas, T. S. Mejia, *et al.*, "Non-classical correlations over 1250 modes between telecom photons and 979-nm photons stored in $^{171}Yb^{3+}$:Y_2SiO_5," Nat. Commun. **13**, 6438 (2022).
52. D. Lago-Rivera, J. V. Rakonjac, S. Grandi, *et al.*, "Long distance multiplexed quantum teleportation from a telecom photon to a solid-state qubit," Nat. Commun. **14**, 1889 (2023).
53. C. Li, S. Zhang, Y. K. Wu, *et al.*, "Multicell atomic quantum memory as a hardware-efficient quantum repeater node," PRX Quantum **2**, 040307 (2021).
54. J. Laurat, C.-W. Chou, H. Deng, *et al.*, "Towards experimental entanglement connection with atomic ensembles in the single excitation regime," New J. Phys. **9**, 207 (2007).
55. M. J. Wang, S. Z. Wang, T. F. Ma, *et al.*, "Generation of highly retrievable atom photon entanglement with a millisecond lifetime via a spatially multiplexed cavity," Quantum **7**, 903 (2023).
56. S.-J. Yang, X.-J. Wang, X.-H. Bao, *et al.*, "An efficient quantum light-matter interface with sub-second lifetime," Nat. Photonics **10**, 381–384 (2016).
57. X.-H. Bao, A. Reingruber, P. Dietrich, *et al.*, "Efficient and long-lived quantum memory with cold atoms inside a ring cavity," Nat. Phys. **8**, 517–521 (2012).
58. M. Wang, H. Jiao, J. Lu, *et al.*, "Cavity-enhanced and spatial-multimode spin-wave-photon quantum interface," arXiv (2023).
59. Á. G. Iñesta, G. Vardoyan, L. Scavuzzo, *et al.*, "Optimal entanglement distribution policies in homogeneous repeater chains with cutoffs," npj Quantum Inf. **9**, 46 (2023).
60. H. de Riedmatten, J. Laurat, C. W. Chou, *et al.*, "Direct measurement of decoherence for entanglement between a photon and stored atomic excitation," Phys. Rev. Lett. **97**, 113603 (2006).
61. Y. Wu, J. Liu, and C. Simon, "Near-term performance of quantum repeaters with imperfect ensemble-based quantum memories," Phys. Rev. A **101**, 042301 (2020).